

学 位 論 文

論文題目

Evaluation of the quantitative performance of non-enhanced dual-energy CT X-map in detecting acute ischemic brain stroke: A model observer study using computer simulation

(非造影 Dual-energy CT X-map による急性期脳虚血領域の検出:
コンピュータ・シミュレーションモデルによる定量的評価)

富山大学医学部 放射線診断・治療学講座

社会人研究生

伊藤 俊英

Abstract

Purpose: A simulation study was performed to evaluate the quantitative performance of X-map images—derived from non-enhanced (NE) dual-energy computed tomography (DECT)—in detecting acute ischemic stroke (AIS) compared with that of NE-DECT mixed images.

Methods: A virtual phantom, 150 mm in diameter, filled with tissues comprising various gray- and white-matter proportions was used to generate pairs of NE-head images at 80 kV and Sn150 kV at three dose levels (20, 40, and 60 mGy). The phantom included an inserted low-contrast object, 15 mm in diameter, with four densities (0%, 5%, 10%, and 15%) mimicking ischemic edema. Mixed and X-map images were generated from these sets of images and compared in terms of detectability of ischemic edema using a channelized Hotelling observer (CHO). The area under the curve (AUC) of the receiver operating characteristic that generated CHO for each condition was used as a figure of merit.

Results: The AUCs of X-map images were always significantly higher than those of mixed images ($P < 0.001$). The improvement in AUC for X-map images compared with that for mixed images at edema densities was 9.2%-12.6% at 20 mGy, 10.1%-17.7% at 40 mGy, and 14.0%-19.4% at 60 mGy. At any edema density, X-map images at 20 mGy resulted in higher AUCs than mixed images acquired at any other dose level ($P < 0.001$), which corresponded to a 66% dose reduction on X-map images.

Conclusions: The simulation study confirmed that NE-DECT X-map images have superior capability of detecting AIS than NE-DECT mixed images.

Key words: Computed tomography (CT), Dual-energy CT, Stroke, X-map

Introduction

Acute ischemic stroke (AIS) is a critical brain disease that is prevalent in developed countries [1]. Rapid and accurate diagnosis of AIS is highly desirable before implementing thrombolytic therapy or mechanical thrombectomy, which helps improve the prognosis of patients with ischemic stroke [2-4].

Magnetic resonance imaging (MRI) is a valuable modality to identify ischemic changes in brain tissue even in their early stages [5]. However, because MRI takes a relatively longer preparation and acquisition time compared with CT and has limited availability, especially during the night shift in hospitals, it is unlikely to be the first method used to evaluate patients with intracranial hemorrhage or suspected ischemic stroke [6]. In contrast, non-enhanced (NE) X-ray CT is a suitable means of ruling out the possibility of a cranial hemorrhage because of its sensitivity. NE-CT is widely available in many institutes and can be easily used to identify ischemic changes in brain tissue during the early stages [4, 5, 7]. However, diagnosis of brain ischemia in the acute stage is a challenge for physicians, the difference in the CT numbers of ischemic changes and those of normal tissue may be in the range of only a few Hounsfield units (HU); additionally, this range is smaller than that for differentiation between gray matter (GM) and white matter (WM) [8, 9].

Dual-energy computed tomography (DECT) has been commercially available since 2010 and has been utilized in many clinical scenarios. In 2016, Noguchi et al. reported the development of the DECT application X-map and its clinical benefits [10]. The X-map can be used to visualize ischemic brain tissue changes without contrast administration. A task-specific, three-material decomposition algorithm suppresses lipid content from voxels of brain tissues and then generates a virtual GM map in which the differences between the GM and the WM are eliminated. As a result, only ischemic edema with lower density than that of normal tissues due to increased water content in the voxels of brain tissue is specifically highlighted, because the background of ischemic edema could be a homogeneous virtual GM.

Since 2016, several groups have reported the utility of DECT to visualize ischemic edema; they employed the same theoretical concept of the X-map algorithms but named

it the “brain edema map,” eliminating the difference between the GM and the WM [11, 12]. They concluded in their clinical studies that such DECT algorithms improved visualization of the early stages of ischemic edema better than mixed images that simulated single-energy (SE) CT images at 120 kV [13]. However, no report has validated the objective detectability of ischemic edema at different edema densities and radiation doses using the X-map and brain edema map.

A human observer study is the usual approach for evaluating task-based diagnostic performance under specific conditions. However, the human observer approach is time-consuming, and it is necessary to carefully control the measurement to obtain accurate results. The channelized Hotelling observer (CHO) has been used in several studies instead of human observers [14-16]. CHO provides an objective method for assessing image quality in lesion detection tasks, such as two-alternative forced choice (2-AFC), by using images for which the signal is accurately known.

Thus, this simulation study aimed to clarify the theoretical validity of the X-map algorithm and evaluated the effectiveness of the X-map algorithm with CHO in detecting ischemic edema by comparing NE-DECT X-map images with NE-DECT mixed images.

This doctoral thesis is based on a paper published in the European Journal of Medical Physics [17].

Materials and Methods

Data acquisition and image reconstruction

A virtual phantom representing the heterogeneity of brain tissues in an adult head was computationally generated. The phantom had a cylindrical shape of 150 mm in diameter and 200 mm in length, was filled with brain tissue, and was surrounded by a 10 mm thick bone. A rod-shaped ischemic lesion 15 mm in diameter and 200 mm in length was placed at the center of the phantom. The edema had four densities (0%, 5%, 10%, and 15% reductions relative to the surrounding brain tissue), representing a progressive increase in water content in the edematous tissue. Human brain tissue consists of the GM and WM, which have complex 3D shapes and combine with each other to form heterogeneous

complex structures. The phantom did not intend to model the entire head, but rather it focused on modeling the local tissues of the brain that underlie ischemic edema. The local tissue was modeled as randomly combined, cloud shapes of textures, which were generated as small variances in the CT number from the mean value of the mixture of the GM and WM (Figure 1). To investigate bias due to heterogeneity of the target brain tissue, image voxels were composed of five GM/WM proportions (0%/100%, 25%/75%, 50%/50%, 75%/25%, and 100%/0%). For instance, GM/WM = 50%/50% indicates that a voxel of tissue contains 50% GM and 50% WM.

An in-house simulation tool that modeled scanner-specific parameters of the third generation dual-source DECT (SOMATOM Force; Siemens Healthineers, Forchheim, Germany)—such as the focal spot size, detector aperture with oversampling, motion of the focal spot on the anode plate of the X-ray tube, polychromatic X-ray spectrum with/without tin-filtration, and scanner geometries—was used to generate projection data of the phantom. The cross-scatter effect from two X-ray tubes is a challenge in dual-source CT scanners and a known cause of inaccurate CT number reproducibility [18, 19]. However, small objects such as the head are relatively less affected by cross-scatter than larger objects such as the body, and advanced correction algorithms can effectively remove both the cross-scatter and the non-cross-scatter effects from images [18-20]. Therefore, no scatter effect was considered in this simulation. Definitions of materials, GM, WM, cortical bone for the skull, and water used for the phantom were obtained from published data [21].

The scan parameters used to create the projection data were in accordance with the vendor's recommended standard NE-DECT protocol for the head (e.g., DE_Head_BrainHem), which uses a pair of tube voltages of 80 kV and 150 kV with tin filtration (Sn150 kV), an X-ray beam width of 32×0.6 mm, and a pitch of 0.7. Radiation dose levels of 20, 40, and 60 mGy in the CT volume dose index ($CTDI_{vol}$) for combined kV was used. These dose levels were determined based on the reference literature, which stated that NE 120 kV head scan protocols use less than 40 mGy for routine scans and 50-60 mGy for stroke scans [22, 23]. Images were reconstructed using a weighted filtered back-projection algorithm [24] with an image matrix of 512×512 , a beam-hardening correction adjusted for the phantom, a reconstruction field of view (FoV) of 240 mm, and

a slice thickness of 5 mm (which is often used for diagnosis), with an increment of 2 mm with at least 50% overlap between adjacent slices, and a standard convolution kernel for the head. The phantom was scanned 50 times for each configuration of edema density and GM/WM proportion to increase the total number of images with various local tissue shapes and textures for CHO because the phantom is randomly generated per scan. For each scan, 20 images located centrally in the longitudinal direction of the phantom were reconstructed and then transferred to DE applications to generate mixed and X-map images. Because the DE application internally performs 3D interpolation of the data volume of 20 stacked images, 10 of the 20 slices, excluding the two ends of the volume (five slices each), were used for the analysis in this study to avoid unstable variations in image characteristics. Thus, a total of 500 images were obtained for each configuration. Images with 0% edema density were considered signal-absent, and images with 5%, 10%, and 15% edema densities were considered signal-present.

Mixed and X-map images

A set of 80 kV and Sn150 kV images was used to generate both mixed and X-map images (Figure 2). An 80 kV image and its corresponding Sn150 kV image were averaged with a weighting factor of 0.5, which is the value recommended by the manufacturer to generate a mixed image that simulates a NE 120 kV SECT image [13, 25].

The X-map image was generated using task-specific, three-material decomposition into water, GM, and WM [10]. As shown in Figure 3, all voxels of brain tissue were projected onto a baseline connected between the water and the GM, along a slope passing through the GM and WM in a spatial domain with Cartesian coordinates of Sn150 kV for the X-axis and 80 kV for the Y-axis. Thus, a virtual GM map (X-map) was obtained. The location of the projected voxel on the baseline reflects the amount of water in each voxel. In clinical cases, voxels of brain tissue without ischemic edema are distributed on a slope according to the GM/WM proportions in each voxel. A voxel located midway between the GM and the WM suggests that the voxel is composed of 50% GM and 50% WM. If the tissue containing the voxel becomes an ischemic edema, the location of the voxel in the diagram will move closer to the water, depending on the percentage of the water in

the voxel. For instance, if a voxel projected on the baseline was exactly halfway between the water and the GM, then the tissue in that voxel contained 50% more water than the normal GM. As a result, the degree of edema was quantified independently of brain tissue heterogeneity. As previously explained, five GM/WM proportions were defined during phantom generation to simulate local tissue properties that accurately reflect the location of corresponding voxels along the slope.

The following settings were used for X-map generation; 2.0 for the slope, 33 HU (= Sn150 kV) and 42 HU (= 80 kV) for the GM, and 29 HU (= Sn150 kV) and 34 HU (= 80 kV) for the WM [10].

All mixed and X-map images were cropped to a matrix of 256×256 pixels at their centers for further analysis to maintain the spatial representations of the images (FoV length [mm] / matrix size [pixel]) between the model observer and the visual interpretation by the human observer.

Edema density analysis

The ischemic edema density in the phantom was specified as a scale of the hypodense contrast values from the background tissue. The accuracy of edema density was evaluated using signal-present images of both the mixed and X-map images. A circular region of interest (ROI) with a diameter of 10 mm was used to measure the mean CT numbers under the ROI at the center (MN_C) of the cropped images and 40 mm away from the center to the north (MN_N), east (MN_E), south (MN_S), and west (MN_W). The measured edema density (ED) was calculated as follows:

$$ED = 1 - \frac{MN_C}{(MN_N + MN_E + MN_S + MN_W)/4} \quad (1)$$

Model observer assessment

Gabor or difference-of-Gaussian (DoG) functions are considered anthropomorphic and are most commonly used as channels for CHO studies [15]. Anthropomorphic channels mimic spatially selective behavior of the human primary visual cortex (V1). To reduce

the complexity of detection tasks against heterogeneous backgrounds, edema signals with a circular cross-section were designed, and the DoG function, which is suitable for detecting a rotationally symmetric object, was used as a channel for CHO to evaluate the detectability of ischemic edema. DoG channels $C_j(\rho)$ are defined in the frequency domain using the following equation:

$$C_j(\rho) = \exp\left(-\frac{1}{2}\left(\frac{\rho}{Q\sigma_j}\right)^2\right) - \exp\left(-\frac{1}{2}\left(\frac{\rho}{\sigma_j}\right)^2\right), \quad (2)$$

where ρ is the spatial frequency variable, σ_j is the standard deviation of j^{th} channel given by $\sigma_j = \sigma_0\alpha^j$, and Q is the channel bandwidth. Ten channels and the same channel parameters proposed by Abbey et al. [16] were used: $\sigma_0 = 0.005$, $\alpha = 1.4$, and $Q = 1.67$. An inverse Fourier transform was applied to the generated channels in the frequency domain to obtain the channels in the spatial domain.

The CHO with DoG channels computed decision variable λ using the following equation.

$$\lambda_j = \boldsymbol{\omega}_{\text{CHO}}^T \cdot (\mathbf{U}^T \cdot \mathbf{g}_j), \quad (3)$$

where \mathbf{U}^T denotes the transposed channel matrix, \mathbf{g} is an image in vector format, j indicates either signal-present (s) or signal-absent (b), and $\boldsymbol{\omega}_{\text{CHO}}^T$ is the transposed CHO template defined by the following equation:

$$\boldsymbol{\omega}_{\text{CHO}} = \left(\frac{1}{2}(\mathbf{K}_{gs} + \mathbf{K}_{gb})\right)^{-1} (\overline{\mathbf{U}^T \mathbf{g}_s} - \overline{\mathbf{U}^T \mathbf{g}_b}), \quad (4)$$

where \mathbf{K}_{gs} and \mathbf{K}_{gb} are the covariances of the channel output for the signals present and absent, respectively. The $\boldsymbol{\omega}_{\text{CHO}}$ is determined by estimating \mathbf{K}_{gs} , \mathbf{K}_{gb} , $\overline{\mathbf{U}^T \mathbf{g}_s}$, and $\overline{\mathbf{U}^T \mathbf{g}_b}$ using the training data. Once the $\boldsymbol{\omega}_{\text{CHO}}$ has been determined, the testing dataset is used to estimate the λ representing the probability of a signal in the image.

In total, 90 2-AFC tasks (five GM/WM proportions, three edema signals, and three dose levels) were generated and applied to the CHO. For each 2-AFC task, the order of “500 signal-present” and “500 signal-absent” images was randomized independently, and they were then split into a set of “300 signal-present” and “300 signal-absent” images for

training and a set of “200 signal-present” and “200 signal-absent” images for testing. A receiver operating characteristic curve was generated and the corresponding area under the curve (AUC) was calculated. Bootstrapping was used to estimate the median and 95% confidence intervals (CI) of the AUC [26].

Data processing and statistical analyses

All image processing in this study, including projection data generation, image reconstruction, mixed image generation, X-map image generation by material decomposition, edema density measurement, and AUC calculation of CHO, was performed using the in-house software developed using MATLAB R2022a (The MathWorks, Natick, MA, USA).

The Mann-Whitney U test was performed to compare the measured edema signal densities and detectability of edema signals in AUCs between the mixed and X-map images. If necessary, Bonferroni correction was applied. Tukey-Kramer post-hoc multiple comparison tests were performed to identify differences in AUCs among the GM/WM proportions for mixed and X-map images independently. A 2-sided *P* value of < 0.05 was considered statistically significant. Statistical analyses were performed using R version 4.2.0 (The R Foundation for Statistical Computing, Vienna, Austria) on RStudio 2022.02.3+492 (RStudio, Boston, MA, USA).

Results

Reproducibility of edema densities

Figure 4 shows measured edema densities calculated using Equation 1 for mixed and X-map images, averaged for all GM/WM proportions. Under overall conditions, measurement errors compared with edema densities when generating 80 kV and Sn150 kV images were approximately $\pm 0.5\%$ (range: -0.53% to 0.47%) for mixed images and approximately $\pm 0.2\%$ (range: -0.23% to 0.1%) for X-map images. Decreasing the radiation dose increased the range of 95% CIs in X-map images. In contrast, the dose did

not affect the range of 95% CIs in mixed images. There was no significant difference in the density of measured edema between the mixed and X-map images at any dose level ($P > 0.05$). Thus, in both mixed and X-map images presented here, all edema densities were accurately reproduced as given densities at all dose levels.

Comparison of detectability between mixed and X-map images

Figure 5 presents the AUCs of all averaged GM/WM proportions for 5%, 10%, and 15% edema densities at 20, 40, and 60 mGy doses each. There were two observations from this figure. First, the AUC tended to increase with increasing dose and increasing edema density in both mixed and X-map images. The AUCs of the X-map images were always significantly higher than those of mixed images in any combination of edema density and dose level ($P < 0.001$). Improvements in the AUC for X-map images compared with that for mixed images at edema densities of 5%, 10%, and 15% were 9.2%, 10.7%, and 12.6%, respectively, at 20 mGy; 10.1%, 15.5%, and 17.7%, respectively, at 40 mGy; and 14.0%, 19.4%, and 19.0%, respectively, at 60 mGy (Table 1).

Second, for each edema density, the AUC of the X-map images at 20 mGy was always significantly higher than that of the mixed images at any dose level ($P < 0.001$). Figure 6 shows the AUCs for all combinations of edema density, GM/WM proportion, and dose levels. The AUCs of the X-map images were always significantly higher than those of the mixed images ($P < 0.001$). In addition, the AUCs of the mixed images tended to increase with increasing percentage of the GM. The AUC of each GM/WM proportion at 15% edema density at 60 mGy, a condition that is less affected by image noise, is presented in detail in Figure 7. There was a clear tendency for AUCs of mixed images to have a positive relationship with the percentage of the GM, and significant differences were identified for AUCs of mixed images between GM/WM proportions 0%/100% and 50%/50% ($P < 0.05$), 0%/100% and 75%/25% ($P < 0.001$), 0%/100% and 100%/0% ($P < 0.001$), and 25%/75% and 100%/0% ($P < 0.05$) (Table 2). However, no such tendency was observed for the AUCs of the X-map images, and there was no significant difference in the AUCs of the X-map images among any of the pairs of GM/WM proportions ($P > 0.05$).

Discussion

I compared the ischemic edema detectability of X-map images with that of mixed images with different edema densities and radiation doses. All edema densities in both the mixed and X-map images were accurately reproduced at given densities at all dose levels in this simulation (Figure 4). There was no statistical difference in edema density between the mixed and X-map images ($P > 0.05$). Therefore, comparing edema detectability between mixed and X-map images in this study was reliable.

Edema detectability assessed with the AUC of X-map images was consistently better than that of mixed images (Figure 5). X-map images improved AUCs by approximately 14% (range: 9.2%-19.4%) on average compared with that by mixed images. Improvements were correlated with edema density and radiation dose because of a relatively higher signal-to-noise ratio with higher edema density and higher dose levels. The major difference between the mixed and X-map images was background heterogeneity due to the GM and the WM. The X-map algorithm flattened that heterogeneity and contributed significantly to improving detectability in X-map images. Assuming that the average CT value of typical GM and WM is approximately 38 HU [9], edema densities of 5%, 10%, and 15% roughly correspond to 2, 4, and 8 HU, respectively. Dzialowski et al. reported, in their experiment using rats, that brain tissue with a decrease >4 HU consistently went into infarction and that minor edema less than 4 HU was difficult to identify by the naked eye [27]. Although it is not appropriate to refer to these results for human studies, it is in agreement with the finding that edema with such small density changes is obscured by the difference between the GM and the WM (~ 7 -10 HU) [8, 9]. Thus, there is a need to identify edema with a density of 10%-15% for reliable diagnosis of AIS in clinical practice. As a rule of thumb, increasing the dose improves low-contrast detectability. Therefore, the radiation dose for AIS scan protocols on NE-CT tends to be higher than that for routine head scan protocols. X-map improved the AUC for an edema density of 10%-15% by approximately 16% at 40 mGy and by 19% at 60 mGy. These results suggest that X-map images can satisfy the potential demand for AIS diagnosis.

In addition, I found that the AUCs of the X-map images at 20 mGy were significantly

higher than those of mixed images at any dose and edema density (Figure 5). This improvement in AUC corresponds to a dose reduction of 66% using X-map images, while ensuring the same level of detectability as mixed images. This dose-reduction capability is particularly beneficial for patients who require several scans for follow-up.

I also found that the trend of detectability of edema in mixed and X-map images differed depending on the GM/WM proportions (Figure 7). In the mixed images, AUC increased monotonically as the percentage of the GM increased. This finding indicates that identifying an ischemic lesion located in the WM is harder than identifying it in the GM. To the best of our knowledge, there are no reports that state that the difficulty of detecting acute ischemia depends on whether the ischemia is in the GM or WM. This finding may explain why interobserver agreements for acute ischemia vary among readers and even among neuroradiologists with specific expertise in AIS diagnosis [28-30]; additionally, the lower interobserver agreement in ASPECT scores for NE-CT also differ compared with ASPECT scores for other modalities [29, 31, 32]. The use of a narrow display window width has been proposed to increase the sensitivity of ischemia detection [5, 33]; however, this is only applicable for images with sufficient radiation doses. Although experience is essential for readers to improve recognition of acute ischemic edema in clinical practice, it is not easy, even for experienced readers, to identify low-density edema [28-30, 33]. In contrast, the ischemic edema detectability of X-map images seems to be independent of the GM/WM proportions, thereby overcoming the limitations of standard CT images. Therefore, NE-DECT X-map can be an alternative to improve the identification and quantification of ischemic edema in AIS, interobserver agreement for NE-CT images, or ASPECT scores for NE-CT [11].

Finally, the aforementioned findings provide a strong incentive to use DECT imaging protocols and the X-map algorithm rather than the traditional NE-CT imaging protocols for the diagnosis of AIS. The same DECT image set acquired for the X-map simultaneously can be utilized for bone-removal DECT application, which specifically removes the skull to highlights small bleeds near the skull that are difficult to identify [34, 35]. This suggests that only single acquisition with the NE-DECT imaging protocols instead of the current standard NE-SECT provide necessary information needed for a one-stop-shop-diagnosis of patient with suspected AIS.

In addition, our findings support the perspective that the X-map algorithm would benefit photon-counting detector CT, which recently became commercially available, because the photon-counting detector CT always acquires spectral data with multiple energy thresholds [36]. Validation of the X-map algorithm with photon-counting detector CT will be a future work.

This study has several limitations. First, although this study was a computer simulation that considers the physical and geometric characteristics of the dual-source CT scanner, the simulated images were not identical to the actual clinical images in terms of the phantom design, which included the GM and WM but not cerebrospinal fluid. In addition, the shape of the phantom was circular, and the skull was thicker, unlike the human head [37]. Other physiological effects, such as brain motion caused by pulsation, were ignored. Consequently, motion artifacts, beam-hardening effects, and noise levels, which are observed on account of the skull, may be different from those in clinical practice. However, the beam-hardening correction was adjusted for the phantom in the image reconstruction to reduce the artifacts effectively. Although the noise level with the phantom was worse than in the clinical practice, the noise distribution was unbiased because of the circular shape of the phantom. Therefore, the results presented in this work tend to underestimate the performance of the X-map algorithm, but it does not overestimate it and is considered to be on the safe side. The phantom design, which included only brain tissue composed of the GM and WM and mimicked the heterogeneity of local tissue, was sufficient to discuss the capability of the X-map algorithm in detecting ischemic edema and to demonstrate the advantages of the X-map algorithm in transforming a heterogeneous background into a homogeneous background to enhance the visibility of ischemic lesions. As aforementioned, a major reason for the difficulty in detecting acute ischemic lesions is the smaller drop in CT number against the background tissue, which is often smaller than the difference in CT number between the GM and the WM. This condition was sufficiently simulated with the phantom so that our results can be translated to clinical practice. As Mangesius et al. indicated, some researchers reported large inter-/intra-patient variations [38]. Based on our result, this is mainly due to the image quality of the acquired data set, not the capability of the X-map algorithm itself.

However, I agree that the ability of the X-map algorithm needs to be evaluated quantitatively in clinical practice as our future work.

Second, advanced reconstruction techniques, such as iterative reconstruction or deep-learning-based reconstruction [39, 40], which are often utilized to reduce image noise or improve the signal-to-noise ratio of objects in clinical practice, have not been used in this study. The X-map algorithm is an image-based material decomposition process that uses the same set of source images to generate mixed images. Neither iterative reconstruction nor deep-learning-based reconstruction can increase the signal intensity of an object; rather, they can only reduce image noise [40]. Therefore, further dose reduction would be possible by applying advanced reconstruction techniques, but it would not affect the evaluation of the X-map algorithm itself by increasing/decreasing detectability. I leave this limitation for clarification in future comprehensive studies. Finally, our study used 80 kV and Sn150 kV as the tube voltage pair, because this is the best kV pair for X-map [10]. However, other kV pairs, such as 90 kV for low kV or Sn140 kV for high kV, may be desired in clinical practice. Similar to other DECT applications, the settings for X-map image generation must be adjusted appropriately for the selected kV-pair. Owing to image noise, detectability can be affected, by choosing the kV-pair in the X-map image. According to Faby et al. [41], when the kV-pair was changed from 80 kV/Sn150 kV to 90 kV/Sn150 kV, to 80 kV/Sn140 kV, and to 80/140 kV, image noise increased by 4%, 10%, and 62%, respectively, which correspond to dose increases of 8%, 17%, and 262%, respectively. The exposure doses used in this study were 20, 40, and 60 mGy, respectively. A dose increases of 8% or 17% was found to be acceptable and had no major influence on our results. However, a 2.6-times higher dose is beyond consideration as it breaks the 20 mGy step. By using tin filtration at high kV, I believe that the results in this paper would be valid. However, this issue can be addressed in our future work.

Conclusions

A computer simulation study was conducted to investigate the performance of the X-map algorithm in detecting acute ischemic edema by comparing NE-DECT X-map images with NE-DECT mixed images, using CHO. X-map images consistently showed better

detectability than mixed images at all edema densities and at all radiation doses. X-map images also allow reduction of the radiation dose by more than 60%, while ensuring the same level of detectability as that of mixed images.

Acknowledgements:

I would like to express my appreciation to Professor Kyo Noguchi, MD, PhD, for his continuous support and thoughtful guidance on this work. I also would like to thank Karl Stierstorfer, PhD, of Siemens Healthineers for his valuable advice on phantom simulation and model observer study.

References

- [1] Phipps MS, Cronin CA. Management of acute ischemic stroke. *BMJ*. 2020;368:l6983.
- [2] National Institute of Neurological Disorders and Stroke rt-PA Stroke Study Group. Tissue plasminogen activator for acute ischemic stroke. *N Engl J Med*. 1995;333:1581-7.
- [3] Saver JL, Goyal M, van der Lugt A, Menon BK, Majoie CB, Dippel DW, et al. Time to Treatment With Endovascular Thrombectomy and Outcomes From Ischemic Stroke: A Meta-analysis. *JAMA*. 2016;316:1279-88.
- [4] Warren DJ, Musson R, Connolly DJ, Griffiths PD, Hoggard N. Imaging in acute ischaemic stroke: essential for modern stroke care. *Postgrad Med J*. 2010;86:409-18.
- [5] Srinivasan A, Goyal M, Al Azri F, Lum C. State-of-the-art imaging of acute stroke. *Radiographics*. 2006;26 Suppl 1:S75-95.
- [6] Rindler RS, Allen JW, Barrow JW, Pradilla G, Barrow DL. Neuroimaging of Intracerebral Hemorrhage. *Neurosurgery*. 2020;86:E414-E23.
- [7] Powers WJ, Rabinstein AA, Ackerson T, Adeoye OM, Bambakidis NC, Becker K, et al. Guidelines for the Early Management of Patients With Acute Ischemic Stroke: 2019 Update to the 2018 Guidelines for the Early Management of Acute Ischemic Stroke: A Guideline for Healthcare Professionals From the American Heart Association/American Stroke Association. *Stroke*. 2019;50:e344-e418.
- [8] Arimitsu T, Di Chiro G, Brooks RA, Smith PB. White-gray matter differentiation in computed tomography. *J Comput Assist Tomogr*. 1977;1:437-42.
- [9] Oh JH, Choi SP, Wee JH, Park JH. Inter-scanner variability in Hounsfield unit measured by CT of the brain and effect on gray-to-white matter ratio. *Am J Emerg Med*. 2019;37:680-4.
- [10] Noguchi K, Itoh T, Naruto N, Takashima S, Tanaka K, Kuroda S. A Novel Imaging Technique (X-Map) to Identify Acute Ischemic Lesions Using Noncontrast Dual-Energy Computed Tomography. *J Stroke Cerebrovasc Dis*. 2017;26:34-41. (Epub: Sep 14, 2016)
- [11] Mohammed MF, Marais O, Min A, Ferguson D, Jalal S, Khosa F, et al. Unenhanced Dual-Energy Computed Tomography: Visualization of Brain Edema. *Invest Radiol*. 2018;53:63-9.
- [12] Grams AE, Djurdjevic T, Rehwald R, Schiestl T, Dazinger F, Steiger R, et al. Improved visualisation of early cerebral infarctions after endovascular stroke therapy using dual-energy computed tomography oedema maps. *Eur Radiol*. 2018;28:4534-41.

- [13] Yu L, Primak AN, Liu X, McCollough CH. Image quality optimization and evaluation of linearly mixed images in dual-source, dual-energy CT. *Med Phys.* 2009;36:1019-24.
- [14] Tseng HW, Fan J, Kupinski MA, Sainath P, Hsieh J. Assessing image quality and dose reduction of a new x-ray computed tomography iterative reconstruction algorithm using model observers. *Med Phys.* 2014;41:071910.
- [15] Barrett HH, Myers KJ, Hoeschen C, Kupinski MA, Little MP. Task-based measures of image quality and their relation to radiation dose and patient risk. *Phys Med Biol.* 2015;60:R1-75.
- [16] Abbey CK, Barrett HH. Human- and model-observer performance in ramp-spectrum noise: effects of regularization and object variability. *J Opt Soc Am A Opt Image Sci Vis.* 2001;18:473-88.
- [17] Itoh T, Noguchi K. Evaluation of the quantitative performance of non-enhanced dual-energy CT X-map in detecting acute ischemic brain stroke: A model observer study using computer simulation. *Phys Med.* 2022;104:85-92.
- [18] Petersilka M, Stierstorfer K, Bruder H, Flohr T. Strategies for scatter correction in dual source CT. *Med Phys.* 2010;37:5971-92.
- [19] Schmidt B, Flohr T. Principles and applications of dual source CT. *Phys Med.* 2020;79:36-46.
- [20] Erath J, Voth T, Maier J, Fournie E, Petersilka M, Stierstorfer K, et al. Deep learning-based forward and cross-scatter correction in dual-source CT. *Med Phys.* 2021;48:4824-42.
- [21] Woodard HQ, White DR. The composition of body tissues. *Br J Radiol.* 1986;59:1209-18.
- [22] Kanal KM, Butler PF, Sengupta D, Bhargavan-Chatfield M, Coombs LP, Morin RL. U.S. Diagnostic Reference Levels and Achievable Doses for 10 Adult CT Examinations. *Radiology.* 2017;284:120-33.
- [23] Paulo G, Damilakis J, Tsapaki V, Schegerer AA, Repussard J, Jaschke W, et al. Diagnostic Reference Levels based on clinical indications in computed tomography: a literature review. *Insights Imaging.* 2020;11:96.
- [24] Stierstorfer K, Rauscher A, Boese J, Bruder H, Schaller S, Flohr T. Weighted FBP--a simple approximate 3D FBP algorithm for multislice spiral CT with good dose usage for arbitrary pitch. *Phys Med Biol.* 2004;49:2209-18.
- [25] Bongers MN, Schabel C, Krauss B, Tsiflikas I, Ketelsen D, Mangold S, et al. Noise-optimized virtual monoenergetic images and iodine maps for the detection of venous thrombosis

in second-generation dual-energy CT (DECT): an ex vivo phantom study. *Eur Radiol.* 2015;25:1655-64.

[26] Efron B, Tibshirani R. The Bootstrap Method for Assessing Statistical Accuracy. *Behaviormetrika.* 1985;12:1-35.

[27] Dzialowski I, Klotz E, Goericke S, Doerfler A, Forsting M, von Kummer R. Ischemic brain tissue water content: CT monitoring during middle cerebral artery occlusion and reperfusion in rats. *Radiology.* 2007;243:720-6.

[28] Grotta JC, Chiu D, Lu M, Patel S, Levine SR, Tilley BC, et al. Agreement and variability in the interpretation of early CT changes in stroke patients qualifying for intravenous rtPA therapy. *Stroke.* 1999;30:1528-33.

[29] Wardlaw JM, Dorman PJ, Lewis SC, Sandercock PA. Can stroke physicians and neuroradiologists identify signs of early cerebral infarction on CT? *J Neurol Neurosurg Psychiatry.* 1999;67:651-3.

[30] Wardlaw JM, Mielke O. Early signs of brain infarction at CT: observer reliability and outcome after thrombolytic treatment--systematic review. *Radiology.* 2005;235:444-53.

[31] Finlayson O, John V, Yeung R, Dowlatshahi D, Howard P, Zhang L, et al. Interobserver agreement of ASPECT score distribution for noncontrast CT, CT angiography, and CT perfusion in acute stroke. *Stroke.* 2013;44:234-6.

[32] Coutts SB, Lev MH, Eliasziw M, Roccatagliata L, Hill MD, Schwamm LH, et al. ASPECTS on CTA source images versus unenhanced CT: added value in predicting final infarct extent and clinical outcome. *Stroke.* 2004;35:2472-6.

[33] Lev MH, Farkas J, Gemmete JJ, Hossain ST, Hunter GJ, Koroshetz WJ, et al. Acute stroke: improved nonenhanced CT detection--benefits of soft-copy interpretation by using variable window width and center level settings. *Radiology.* 1999;213:150-5.

[34] Potter CA, Sodickson AD. Dual-Energy CT in Emergency Neuroimaging: Added Value and Novel Applications. *Radiographics.* 2016;36:2186-98.

[35] Naruto N, Tannai H, Nishikawa K, Yamagishi K, Hashimoto M, Kawabe H, et al. Dual-energy bone removal computed tomography (BRCT): preliminary report of efficacy of acute intracranial hemorrhage detection. *Emerg Radiol.* 2018;25:29-33.

[36] Flohr T, Petersilka M, Henning A, Ulzheimer S, Ferda J, Schmidt B. Photon-counting CT review. *Phys Med.* 2020;79:126-36.

- [37] Lillie EM, Urban JE, Lynch SK, Weaver AA, Stitzel JD. Evaluation of Skull Cortical Thickness Changes With Age and Sex From Computed Tomography Scans. *J Bone Miner Res.* 2016;31:299-307.
- [38] Mangesius S, Janjic T, Steiger R, Haider L, Rehwald R, Knoflach M, et al. Dual-energy computed tomography in acute ischemic stroke: state-of-the-art. *Eur Radiol.* 2021;31:4138-47.
- [39] Lell MM, Wildberger JE, Alkadhi H, Damilakis J, Kachelriess M. Evolution in Computed Tomography: The Battle for Speed and Dose. *Invest Radiol.* 2015;50:629-44.
- [40] Alagic Z, Diaz Cardenas J, Halldorsson K, Grozman V, Wallgren S, Suzuki C, et al. Deep learning versus iterative image reconstruction algorithm for head CT in trauma. *Emerg Radiol.* 2022;29:339-52.
- [41] Faby S, Kuchenbecker S, Sawall S, Simons D, Schlemmer HP, Lell M, et al. Performance of today's dual energy CT and future multi energy CT in virtual non-contrast imaging and in iodine quantification: A simulation study. *Med Phys.* 2015;42:4349-66.

Figure Legends

Figure 1: Example of a cross-sectional view of a phantom without edema signal. The brain tissue is formed by a combination of randomly generated cloud shapes, producing a heterogeneous texture. The texture was defined by the mean CT number according to the GM/WM proportion and its variance (one standard deviation in our phantom). (A) Schematic of the cross section, with the contours representing the distribution of CT numbers; the mean value of the GM/WM proportion (e.g., 32 HU) is shown as a thick line and the variance as a thin line. (B) Image corresponding to the schema in the left. The dashed rectangle is a region of interest (256×256 pixels) to be cropped out for analysis.

Figure 2: Sample images with a 5% edema. (A) and (D), (B) and (E), (C) and (F) Sets of mixed and X-map images, respectively, generated from the same 80 kV and Sn150 kV data sets at 40 mGy, with a display window level/width setting of 34/40 HU. The GM/WM proportions are 0%/100% for (A) and (D), 50%/50% for (B) and (E), and 100%/0% for (C) and (F).

Figure 3: Principle of the X-map algorithm described using dual-energy diagram. All voxels of brain tissue were projected onto a baseline that connected between the water and the GM, along a slope that passed through the GM and WM. A virtual GM map (X-map) was thus obtained. The dots distributed around the slope are examples of voxels of normal brain tissue in a clinical data. The actual clinical data are not polarized to the nominal points of GM and WM.

Figure 4: Measured edema densities in mixed and X-map images with averaged GM/WM proportions at different doses for (A) 5%, (B) 10%, and (C) 15% edema densities. Error bars represent 95% confidence intervals of measurements.

Figure 5: AUC values averaged for all GM/WM proportions in mixed and X-map images. Error bars represent 95% confidence intervals of AUC values. Asterisks (*) indicate statistically significant differences.

Figure 6: AUC values in mixed and X-map images with different GM/WM proportions at different radiation doses. (A), (B), and (C) exhibit edema densities of 5%, 10%, and 15%, respectively. Error bars represent 95% confidence intervals of AUC values. Asterisks (*) indicate statistically significant differences.

Figure 7: AUC values for GM/WM proportions with 15% edema density at 60 mGy (rearranged data from Figure 6). Error bars represent 95% confidence intervals of AUC values. Asterisks (*) indicate statistically significant differences.

Table 1: Relative detectability for averaged GM/WM proportions of X-map to mixed images

Dose (mGy)	Edema Density (%)	Relative AUC of X-map to mixed images	
		Median	(95% CI)
20	5	9.2%	(7.8%-10.5%)
	10	10.7%	(9.4%-11.9%)
	15	12.6%	(11.5%-13.6%)
40	5	10.1%	(8.8%-11.4%)
	10	15.5%	(14.5%-16.6%)
	15	17.7%	(16.8%-18.7%)
60	5	14.0%	(12.8%-15.2%)
	10	19.4%	(18.4%-20.4%)
	15	19.0%	(18.2%-19.9%)

GM: gray matter; WM: white matter; AUC: area under the curve

Table 2: Detectability for mixed images and for X-map images (15% edema density at 60 mGy)

GM/WM Proportion (%)	AUC		P-value (*<0.05, **<0.001)					
	Median	(95% CI)	0/100	25/75	50/50	75/25	100/0	
0/100	0.754	(0.744-0.761)	---	0.3560	0.0230*	0.0006**	0.0000**	
25/75	0.768	(0.756-0.777)	---	---	0.7578	0.1770	0.0024*	
50/50	0.772	(0.763-0.781)	---	---	---	0.8423	0.0893	
75/25	0.781	(0.768-0.792)	---	---	---	---	0.5679	
100/0	0.790	(0.781-0.800)	---	---	---	---	---	
X-map Images	0/100	0.923	(0.744-0.761)	---	0.9823	0.6727	0.2792	0.9745
	25/75	0.920	(0.756-0.777)	---	---	0.9352	0.6071	1.0000
	50/50	0.916	(0.763-0.781)	---	---	---	0.9667	0.9501
	75/25	0.914	(0.768-0.792)	---	---	---	---	0.6436
100/0	0.921	(0.781-0.800)	---	---	---	---	---	

GM: gray matter; WM: white matter; AUC: area under the curve; CI: confidence interval

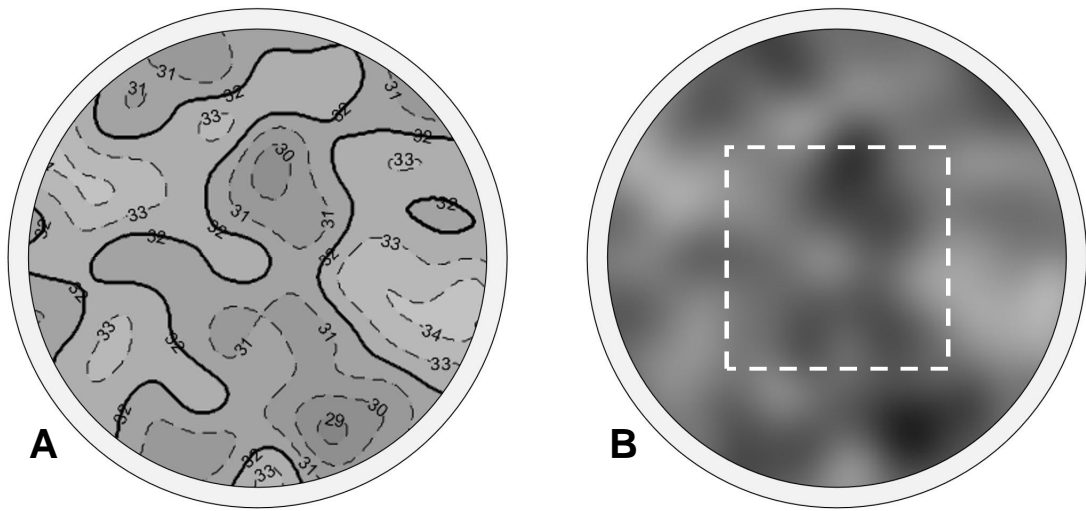


Figure 1

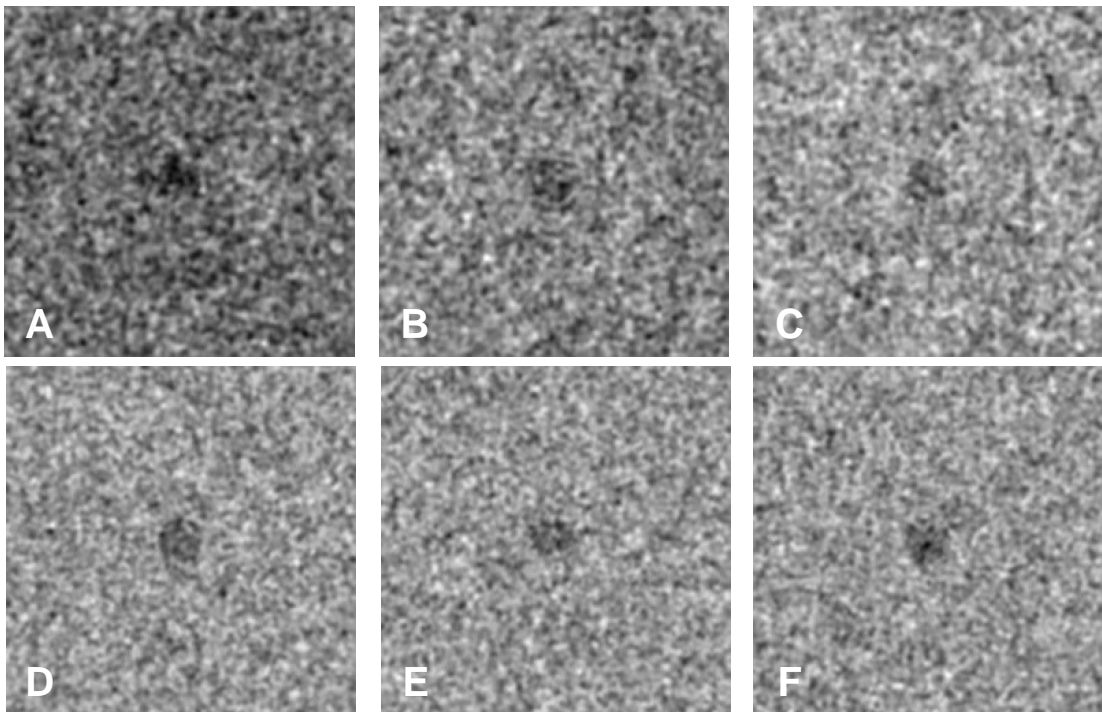


Figure 2

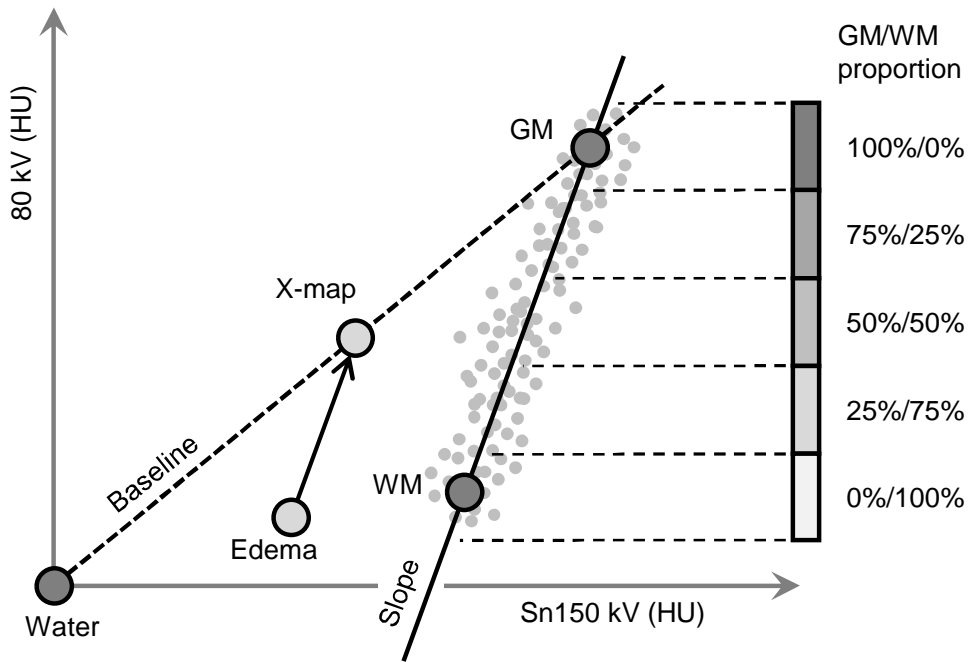


Figure 3

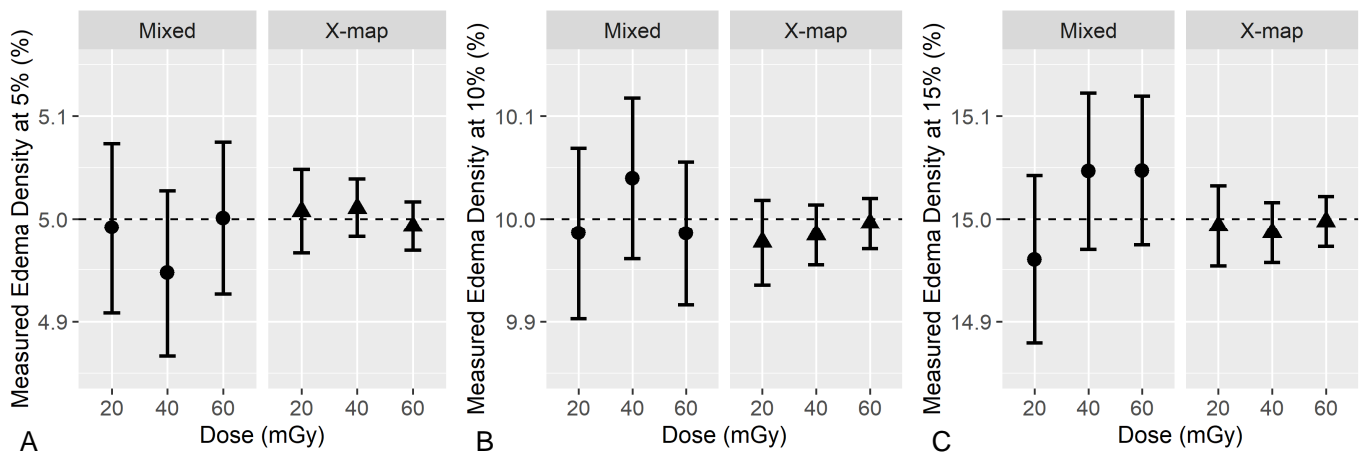


Figure 4

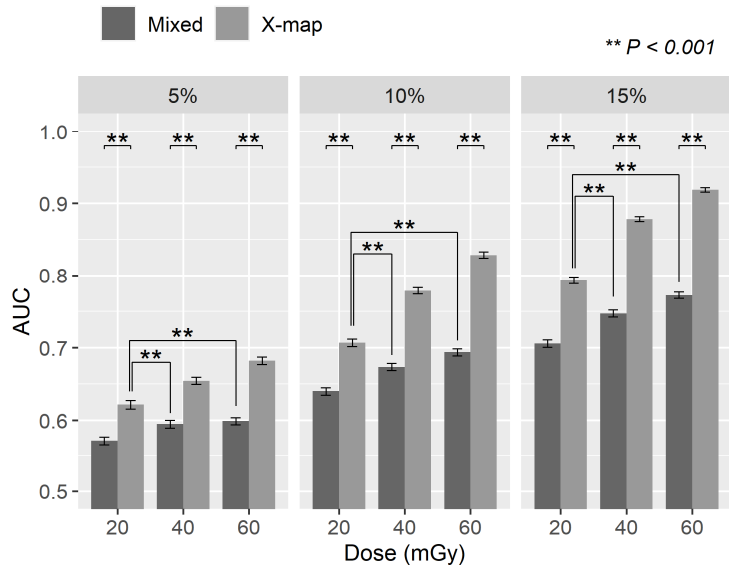


Figure 5

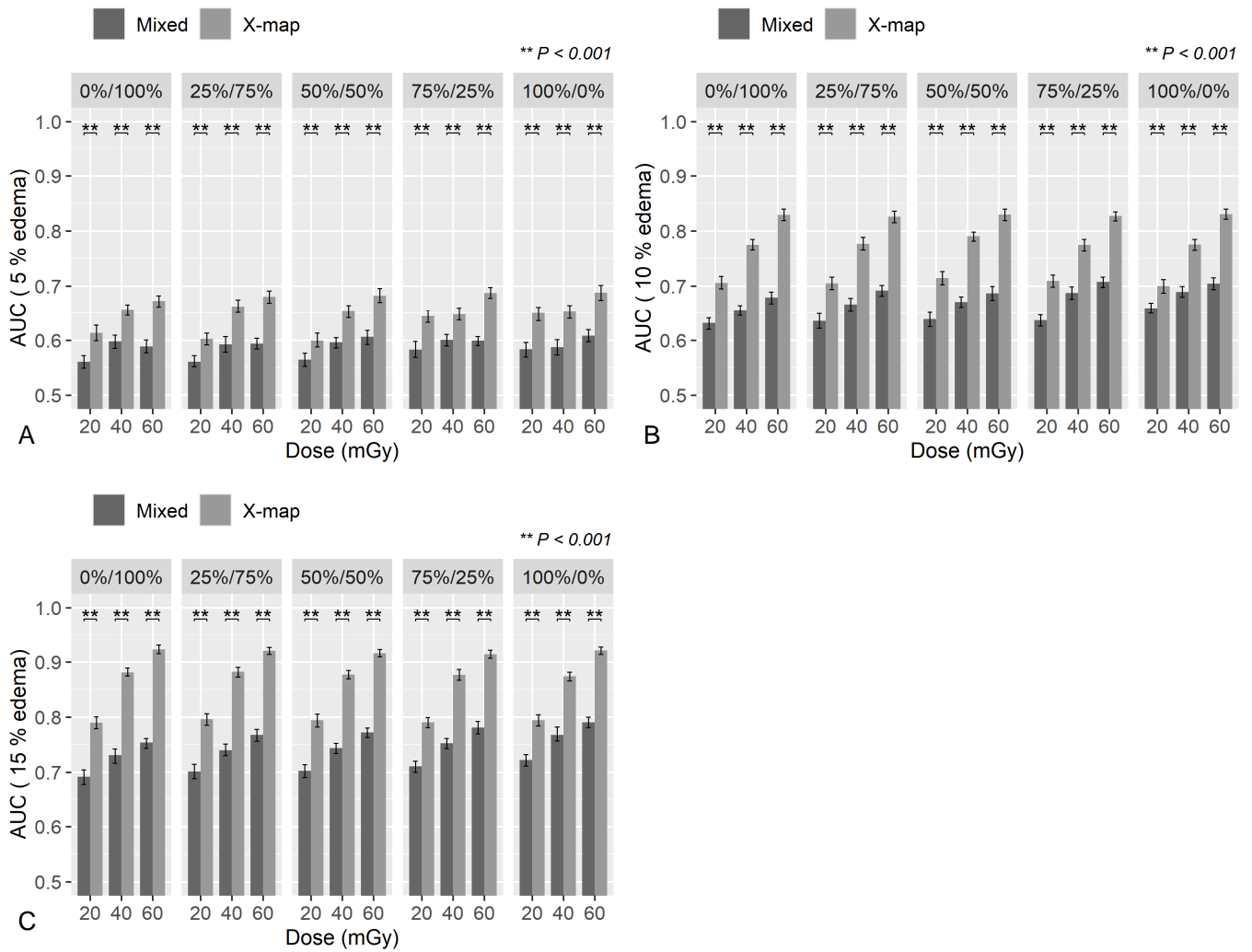


Figure 6

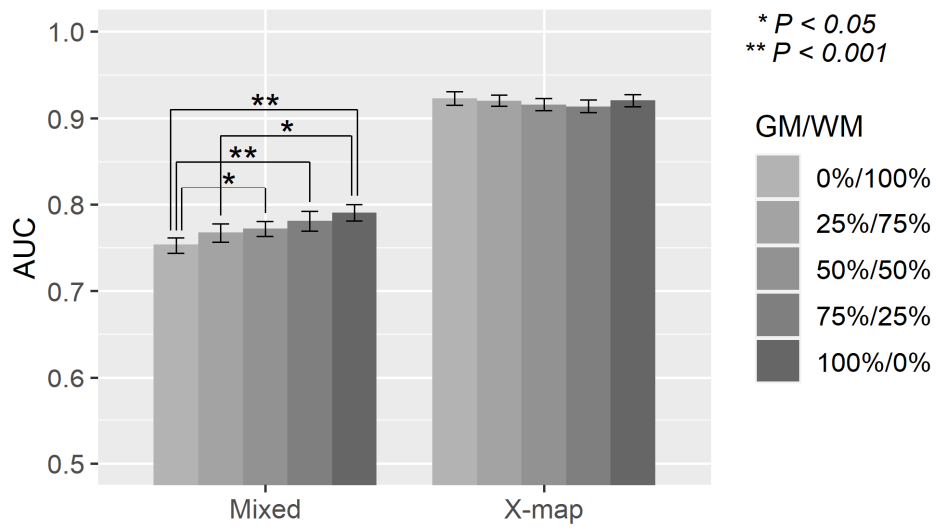


Figure 7